Origin of high Zn contents in Jurassic limestone of the Jura mountain range and the Burgundy

Evidence from Zn speciation and distribution

Journal Article

Author(s):
Jacquat, Olivier; Rambeau, Claire; Voegelin, Andreas; Efimenko, Natalia; Villard, André; Föllmi, Karl B.; Kretzschmar, Ruben

Origin of high Zn contents in Jurassic limestone of the Jura mountain range and the Burgundy: evidence from Zn speciation and distribution

Olivier Jacquat · Claire Rambeau · Andreas Voegelin · Natalia Efimenko · André Villard · Karl B. Föllmi · Ruben Kretzschmar

Abstract In order to better understand the origin and enrichment mechanisms leading to elevated Zn concentrations in Jurassic limestone of the Jura mountain range (JMR) and the Burgundy (B), we investigated four locations of Bajocian age (JMR: Lausen–Schleifenberg, Gurnigel; B: Vergisson–Davayé, Lucy-le-Bois) and two locations of Oxfordian age (JMR: Dornach, Pichoux) for their Zn distribution and speciation. Measurements of the acid-extractable and bulk Zn contents showed that Zn is stratigraphically and spatially heterogeneously distributed, in association with permeable carbonate levels. Up to 3,580 and 207 mg/kg Zn was detected in Bajocian and Oxfordian limestone, respectively, with numerous limestone samples having Zn contents above 50 mg/kg. Using X-ray absorption near edge structure spectroscopy and micro-X-ray fluorescence spectrometry, the speciation and micro-scale distribution of Zn was investigated for selected limestone samples. In Bajocian limestone sphalerite and/or Zn-substituted goethite and a minor fraction of Zn-bearing carbonates were identified. In contrast, Zn-bearing carbonates (Zn-substituted calcite and hydrozincite) were accounting for most of the total Zn in Oxfordian limestone. The micro-scale distribution of Zn for Bajocian and Oxfordian limestone was however similar with localized Zn-rich zones in the limestone cement and at the rim of oolites. The stratigraphic sporadicity and microscale heterogeneity of the Zn distribution together with the Zn speciation results point to a hydrothermal origin of Zn. Occurence of Zn-goethite is probably linked to the oxidative transformation of framboidal pyrite and hydrothermal sphalerite in contact with meteoritic waters. Difference in speciation between Bajocian limestone and Oxfordian limestone may be related to differences in rock permeability

O. Jacquat · R. Kretzschmar
Department of Environmental Sciences,
Institute of Biogeochemistry and Pollutant Dynamics,
ETH Zurich, CHN, 8092 Zurich, Switzerland

C. Rambeau · N. Efimenko · A. Villard · K. B. Föllmi
Institute of Geology, University of Neuchâtel,
2000 Neuchâtel, Switzerland

A. Voegelin
Eawag, Swiss Federal Institute of Aquatic Science and
Technology, Überlandstrasse 133, 8600 Dübendorf, Switzerland

Present Address:
O. Jacquat (✉)
Swiss Federal Office for the Environment,
3003 Bern, Switzerland
e-mail: olivier.jacquat@bafu.admin.ch

Present Address:
C. Rambeau
Institute of Plant Sciences, University of Bern,
3013 Bern, Switzerland

Present Address:
N. Efimenko · K. B. Föllmi
Institute of Geology and Palaeontology,
University of Lausanne, Anthropole,
1015 Lausanne, Switzerland

and/or to various hydrothermal events. Isotopic dating of the different mineralizations will be needed to decipher differences in Zn speciation and the precise chronology of hydrothermal episodes.

1 Introduction

Jurassic limestone of the Jura mountain range (JMR) and the Burgundy bear anomalously high zinc (Zn) and cadmium (Cd) concentrations (Baize and Sterckeman 2001; Dubois et al. 2002; Jacquat et al. 2009a; Laveuf et al. 2009; Quezada-Hinojosa et al. 2009; Rambeau et al. 2010). Up to 92 mg/kg Zn and 21 mg/kg Cd have been reported for limestone of Bajocian age and up to 207 mg/kg Zn and 1 mg/kg Cd for limestone of Oxfordian age (Jacquat et al. 2009a; Rambeau 2006), whereas mean Zn and Cd contents in marine carbonate rocks are considered to be close to 20 and 0.03 mg/kg, respectively (Alloway 1995; Tuchschmid 1995). As a consequence, numerous soils in the Burgundy and the JMR were identified to be naturally enriched with Zn and Cd originating from the parent rock (Baize and Sterckeman 2001; Dubois et al. 2002; Jacquat et al. 2009a; Laveuf et al. 2009; Rambeau et al. 2010). The origin of elevated Zn (and Cd) contents in the limestone however is still unclear.

The stratigraphy and paleogeography of the Jurassic limestone of the JMR and the Burgundy have been intensively studied. In this period, a shallow carbonate platform (Burgundy platform or "plate-forme Septentrionale") developed in a subtropical climate near the southern European margin of the northern Tethyan, covered by an epicontinental sea. This shallow-marine carbonate platform from which the investigated limestone originate was bordered to the east by the Swabian realm, to the west by the Paris basin and extended southward to the marginal basins of the opening Tethys (Fig. 1). Bajocian to Bathonian sediments consist of oolitic carbonate (Hauptrogenstein formation, Celtic realm, domain west of the today's Aare river, Gonzalez and Wetzel 1996, and references therein), whereas sediments of the Oxfordian are characterized by bioclastic carbonates intercalated with episodic siliciclastic sediments (Hug 2003, and references therein). These Jurassic sediments experienced two burial phases during the Cretaceous and the Miocene, with maximum burial depth of about 1,000 m below sea level and burial temperature reaching a maximum of 70°C during the Late Cretaceous (Elie and Mazurek 2008; Mazurek et al. 2006; Timar-Geng et al. 2006). Also, two phases of uplift with meteoric water inputs during Early Cretaceous (Barremian

and Aptian/Albian, respectively) affected the Jurassic limestone of the Burgundy platform (Brigaud et al. 2009). As a consequence of a related extensive cementation, these rocks usually display low porosity and permeability (porosity < 15%, permeability > 0.5 mD, Brigaud et al. 2009; Chevalier et al. 2010).

Information on the speciation (i.e., chemical form) of Zn in limestone may contribute to a better understanding of the origin of Zn enrichments. However, determination of the speciation of Zn in rocks with less than ~ 10 g/kg of Zn using conventional mineralogical techniques such as bulk X-ray diffraction is hardly feasible. Synchrotron-based X-ray absorption spectroscopy (XAS), on the other hand, is an element-specific spectroscopic technique that provides information on the local coordination and speciation of an element even at low concentrations in complex geological samples. XAS spectra are subdivided into two spectral regions: The X-ray absorption near edge structure (XANES) around the absorption edge and the extended X-ray absorption fine structure (EXAFS) well above the edge (Koningsberger and Prins 1988). The XANES spectrum bears information on the valence and coordination geometry and the EXAFS spectrum on the type, number, and distance of neighboring atoms. In the case of natural samples that may contain a specific element in different chemical forms, linear combination fitting (LCF) can be used to identify and quantify the different chemical phases on the basis of a reference spectra database (Kelly et al. 2008; Manceau et al. 2002). Because of the higher signal intensity in the XANES than in the EXAFS region, collection of the XANES signal is less time-consuming and better suited for samples with minor quantities of the element of interest.

The aim of the current study was to contribute to a better understanding of the enrichment mechanisms leading to locally elevated Zn concentrations in Jurassic limestone of the Burgundy and the JMR by (1) determining the concentration and distribution of Zn in Bajocian and Oxfordian sediments from several locations and (2) investigating the micro-scale distribution and speciation of Zn using bulk and micro-focused X-ray fluorescence spectrometry (XRF) and XANES spectroscopy.

2 Materials and methods

2.1 Geological settings of sampling sites

The stratigraphic sections and sampling sites described below have been previously been studied (Hug 2003; Jacquat et al. 2009a; Rambeau 2006). Samples collected from these earlier studies were investigated in the present work. The stratigraphic sections Lausen–Schleifenberg,
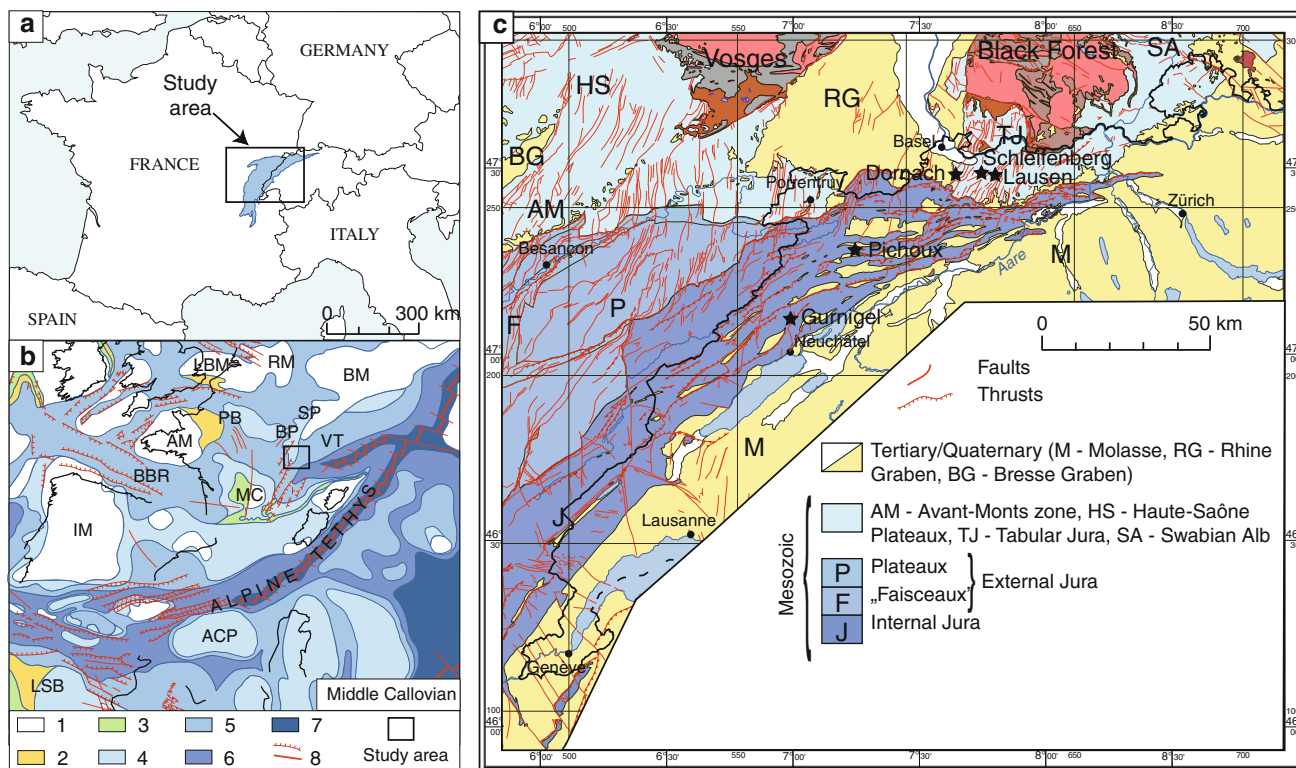
Fig. 1 Study area. **a** Location of the Jura Mountains and Burgundy. **b** Paleogeographic position of the studied area during the Middle Callovian (after Thierry and Barrier 2000). Depositional environments: *1* emerged areas (assumed and ascertained), *2* deltaic shallow marine (terrigenous), *3* shallow environments with fluctuating salinities, *4* shallow marine carbonate deposits, *5* deep(er) carbonates, (hemi)pelagic oozes, *6* deep marine, *7* deep oceanic basins, *8*

unspecified faults and normal faults. *ACP* Apennine Carbonate Platform, *AM* Armorican Massif, *BBR* Bay of Biscay Rift, *BM* Bohemian Massif, *BP* Burgundy Platform, *IM* Iberian Massif, *MC* Massif Central, *LBM* London Brabant Massif, *LSB* Lower Sahara Basin, *PB* Paris Basin, *RM* Rhenish Massif, *SP* Swabian Platform, *VT* Valais Trough. **c** Regional tectonic map of the northeastern Jura Mountains with samples location (after Spicher 2005)
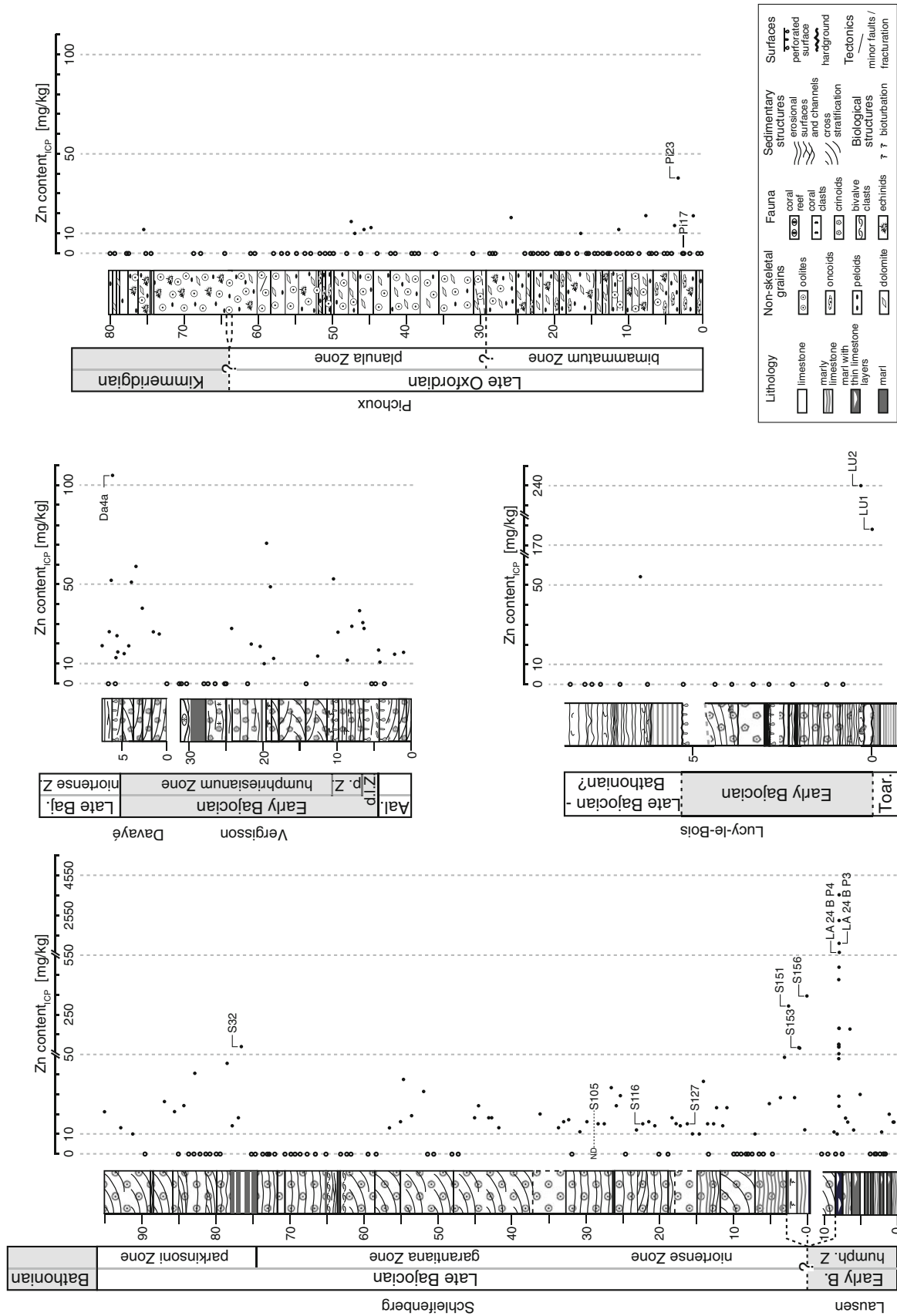
Vergisson–Davayé, Lucy-le-Bois and Gorges du Pichoux are depicted in Fig. 2.

2.1.1 Lausen–Schleifenberg (Jura mountain range, Bajocian)

The lower 5 m of this composite section crops out in a quarry near the village of Lausen (47°28′N, 7°46′E), and the upper 95 m of the carbonate succession on the slope of the hill Schleifenberg close to the nearby city of Liestal, Canton Baselland, Switzerland (47°29′N, 7°44′E). The lithology of the Lausen–Schleifenberg composite section predominantly consists of oolitic and locally bioclastic grainstone and packstone, which were deposited during the Early to Late Bajocian in the southeastern part of the Burgundy platform (Gonzalez and Wetzel 1996; Quezada-Hinojosa et al. 2009). Two major marly intervals characterize the upper part (*humphriesianum* ammonite Zone) of the Lausen section and the upper part (*parkinsoni* ammonite Zone) of the Schleifenberg section and consist of blue marl and red–yellow–gray marl intercalated with oolitic packstone, respectively. Inside thick oolitic

grainstone beds cross-stratification patterns were observed. Erosional surfaces and channel infills separate thin layers of packstone.

2.1.2 Gurnigel (Jura mountain range, Bajocian)

The oolitic bioclastic limestone GUR (Late Bajocian) corresponds to the bedrock horizon of a soil profile located near the pass of la Vue des Alpes, Canton Neuchâtel (Le Gurnigel, 47°05′N, 6°54′E), which has been described in detail elsewhere (Jacquat et al. 2009a, not shown on Fig. 2).

2.1.3 Vergisson–Davayé (Burgundy, Bajocian)

The Vergisson–Davayé section is located near Mâcon, Burgundy. The lower part of this composite section crops out on the Vergisson cliff (46°18′N, 4°43′E), whereas the upper part is situated in a former quarry near the village of Davayé (46°18′N, 4°44′E). The total section is about 39 m thick, ranging from latest Aalenian to earliest Late Bajocian (Thiry-Bastien 2002). The carbonate successions have

Fig. 2 Sections of Lausen–Schleifenberg, Vergisson–Davayé, Lucy-le-Bois and Pichoux and corresponding concentration profiles for acid-extractable Zn (measured by ICP-MS); *open circles* at ZnICP = 0 represent samples with Zn content below the detection limit (10 mg/kg)

been deposited in the southwestern part of the Burgundy platform (Gonzalez and Wetzel 1996) and are dominated by bioclastic limestone, mainly composed of debris of echinoderms, molluscs and brachiopods. The lower part of the Vergisson section is composed of reddish, crinoid-rich grainstone of Late Aalenian. Intercalations of nodular crinoid- and bioclast-rich packstone and of thin red marly levels are subsequently observed, corresponding to the *discites* and *propinquans* ammonite Zones of the Early Bajocian. Crinoid-rich grainstone characterized by cross-stratification patterns followed by grainstone rich in crinoids and coral clasts were deposited during the *humphriesianum* ammonite Zone. The top of the Vergisson section is composed of packstone rich in crinoids and coral clasts, marly levels and a small coral bioherm. The Davayé section consists of a succession of reddish crinoidal grainstone/packstone, which are laterally equivalent to the top of the Vergisson section and correspond to the end of the *humphriesianum* ammonite Zone. These carbonates are covered by siliciclastic crinoid-rich gray packstone of Late Bajocian age (*niortense* ammonite Zone) featuring erosional surfaces and channels.

2.1.4 Lucy-le-Bois (Burgundy, Bajocian)

The section of Lucy-le-Bois (47°33′N, 3°53′E) is about 8.5 m thick and crops out in a former quarry near the village of Lucy-le-Bois in Burgundy, France. The condensed carbonate layers were deposited in the western part of the Burgundy platform (Gonzalez and Wetzel 1996) and are dated as latest Toarcian to Late Bajocian/Bathonian (Mégnien et al. 1971). Deposits of Aalenian and probably earliest Bajocian age are missing. The lower part of the section is characterized by reddish, crinoid-rich packstone to grainstone levels of Early Bajocian age, which are locally rich in bioclasts, and separated by erosional surfaces and channels. These deposits are followed by marly layers and crinoidal grainstone beds characterized by cross-stratification patterns. This succession ends with an erosional surface, overlapped by marly deposits and siliceous grey packstone of Late Bajocian to Bathonian age.

2.1.5 Dornach (Jura mountain range, Oxfordian)

The limestone sample DOR was collected from the bedrock horizon of a previously described soil profile (Jacquat et al. 2009a). The profile is located south of the village of

Dornach, Canton Solothurn (47°28′N, 7°37′E), not shown on Fig. 2. The bedrock consists of oolitic, bioclastic and micritic limestone of Late Oxfordian age.

2.1.6 Gorges du Pichoux (Jura mountain range, Oxfordian)

The Gorges du Pichoux section is located between the villages Sornetan and Undervelier (47°17′N, 7°13′E), Switzerland. The section has previously been described in detail (Hug 2003). Briefly, the 80 m thick calcareous succession spans the time interval from the Late Oxfordian (*binammatum* and *planula* ammonite Zone) to the Early Kimmeridgian. The base of the section consists of lagoonal sediments with oncoids, followed by beds richer in oolites and quartz, with fluctuating evaporitic contents. After a few centimeters thick level of black oolite, the sediment becomes marlier for a few meters. Above follows thin layers of limestone partly affected by dolomitization and rich in oncoids, gastropods and coral fragments. The overlying thicker beds are mainly composed of oolitic grainstone alternating with peloidal micritic facies. At the top of the section, the dominance of peloid-rich limestone indicates a facies change towards a lower energy system.

2.2 Sample preparation and determination of element contents

Powdered rock samples for determination of element contents and bulk XAS analysis were prepared using a vibratory agate disc mill.

For the determination of acid-extractable Zn contents, about 250 mg of powdered limestone were suspended in 10 mL 65% HNO_3 (Suprapur, Merck, Nr. 100441). The suspensions were digested in a microwave oven at 180°C during 10 min. After cooling, the supernatants were filtered (0.45 μm). The filtered solutions were diluted with doubly deionized water for analysis by inductively coupled plasma-mass spectrometry (ICP-MS, Perkin Elmer Elan 6100, standard deviation from multiple measurements 4 mg/kg). Rhodium was used as internal standard to correct for matrix effects and instrumental drift. Note that the extent to which Zn is released during acid digestion strongly depends on its speciation. Zn-bearing carbonates will be totally extracted, but other Zn-bearing minerals including phyllosilicates, oxides and sulfides may only be partly dissolved by this extraction (Gleyzes et al. 2002; Voegelin et al. 2008).

Total element contents of selected limestone samples were determined by energy-dispersive XRF (Spectro X-Lab 2000). Pellets for XRF analysis were prepared from 4 g of powdered sample mixed with 0.9 g of wax (Licowax). Analysis of reference materials with certified Zn

contents of 509 and 7,290 mg/kg returned 513 ± 18 and $7,516 \pm 44$ mg/kg Zn ($\pm$standard deviation, $n = 14$).

The limestone samples were classified based on the analysis of sedimentary facies and structures in outcrops. Microfacies were determined on polished uncovered glass-supported thin-sections using a polarized light microscope.

2.3 Synchrotron-based bulk and microfocused analyses

Bulk Zn K-edge XANES spectra of powdered rock samples were recorded at the XAS beamline at the Angströmquelle Karlsruhe (ANKA, Karlsruhe, Germany). The monochromator was energy-calibrated by setting the first inflection point of the absorption edge of a metallic Zn foil to 9,659.0 eV. Sample powders were mixed with wax (Licowax) and pressed into 13-mm pellets. The pellets were analyzed at room temperature in fluorescence mode using a 5-element Ge solid state detector.

Spatial element distribution and local Zn speciation in thin-sections from limestone S151 (150 μm thick), GUR (200 μm thick) and DOR (30 μm thick) were analyzed by microfocused XRF spectrometry (μ-XRF) and XANES spectroscopy (μ-XANES) at beamline 10.3.2 at the Advanced Light Source (ALS), Berkeley, USA (Marcus et al. 2004). The rock sections were mounted in a 45° angle to the incident beam, and the fluorescence signal was recorded at an angle of 90° using a 7-element Ge solid state detector. The μ-XRF maps were obtained by scanning the samples at an incident photon energy of 10 keV with a step size of 20×20 μm^2 and dwell times of 200 (DOR), 100 (S151) or 50 (GUR) ms/point. The black-white scale of the XRF maps for Zn and Fe was defined to cover the range between the lowest single pixel value (black) and the 90 percentile of all pixel values (white). At selected points-of-interest (POI), μ-XANES spectra at the Zn K-edge were measured using a beam size between 5×5 and 16×7 μm^2 (depending on the size of the feature of interest).

Extraction of the normalized XANES spectra from raw data was performed using the software code Athena (Ravel and Newville 2005). E_0 was fixed to 9,663.0 eV and spectra were normalized by fitting a first order polynomial to the data up to 30 eV below the edge and a second order polynomial to the data from 150 to 380 eV above the edge.

2.4 Analysis of Zn K-edge XANES data

All XANES spectra collected on bulk samples and thin sections were combined for evaluation by principal component analysis (PCA) using the software code SIXpack (Webb 2005). The number of spectral components required to reproduce the entire data set without experimental noise was determined based on the empirical indicator (IND) function (Malinowski 1977; Manceau et al. 2003). To identify suitable reference spectra for data analysis by LCF, target testing (TT) was then performed on a large database of reference spectra of synthetic (syn.) and natural (nat.) minerals and precipitates used in previous work (Jacquat et al. 2008, 2009a, b, c), including an additional reference spectrum of wurtzite (Beauchemin et al. 2004). The empirical SPOIL value (Malinowski 1978) and the normalized sum of squared residuals (NSSR = $(\Sigma_i(E_{exp} - E_{fit})^2)/\Sigma_i(E_{exp})^2$) of the target transforms were used to judge the suitability of reference spectra for LCF (Isaure et al. 2002; Jacquat et al. 2009c; Kirpichtchikova et al. 2006; Panfili et al. 2005; Sarret et al. 2004). LCF analysis was performed over the energy range 9,643–9,743 eV (-20 to $+80$ eV around E_0 fixed at 9,663 eV) and was carried using software from beamline 10.3.2 at the Advanced Light Source (Marcus et al. 2004).

3 Results

3.1 Zn contents in limestone

The acid-extractable Zn contents of samples from the sections Lausen–Schleifenberg, Vergisson–Davayé, Lucy-le-Bois and Pichoux are presented in Fig. 2 and in Table 1 as well as Tables EA1–EA6 in the electronic annex. In the Bajocian sections Lausen–Schleifenberg, Vergisson–Davayé and Lucy-le-Bois (i.e., all Bajocian sections), acid-extractable Zn was stratigraphically inhomogeneously distributed, i.e., occurred in distinct levels. Highest acid-extractable Zn contents and largest variations were observed in limestone levels, whereas concentrations of acid-extractable Zn in the marly beds fell below detection limit. Oolitic and bioclastic limestone with high acid-extractable Zn contents [i.e., above the 80-percentile level ($n = 37$) of 48 mg/kg total Zn reported for limestone from Switzerland (Tuchschmid 1995)] were mainly located close to the boundary between Early Bajocian (*humphriesianum* ammonite Zone) and Late Bajocian (*niortense* ammonite Zone). Also within single limestone beds, large variations in acid-extractable Zn contents were observed, pointing towards stratigraphically as well as spatially highly inhomogeneous Zn distribution. In the second last oolitic limestone level (La24) of the Lausen section, for example, acid-extractable Zn of samples collected at different locations of the same bed ranged from 24 to 3,580 mg/kg. The samples from the Pichoux section of Oxfordian age exhibited little variations in their acid-extractable Zn contents, with concentrations typically below the detection limit of 10 mg/kg and a maximum concentration of 38 mg/kg (sample Pi23).

Based on acid-extractable Zn contents (Fig. 2, Online Resource 1, Tables OR1–6), several limestone samples with low and high Zn contents from the Lausen–Schleifenberg, Vergisson–Davayé, Lucy-le-Bois and Pichoux sections were

Table 1 Geological characteristics for selected limestone samples, total content of Zn, Cd, S, Fe, Si and Ca determined by bulk XRF-spectrometry (X_{tot}), and acid-extractable contents of Zn and Cd (X_{ICP})

Sample[a]	Age[b]	Origin[c]	Facies	Zn_{tot} (mg/kg)	Zn_{ICP} (mg/kg)	Cd_{tot} (mg/kg)	Cd_{ICP} (mg/kg)	S_{tot} (mg/kg)	Fe_{tot} (mg/kg)	Si_{tot} (mg/kg)	Ca_{tot} (mg/kg)
S32	La. Bajocian	Jura BL	Oosparite	92	95	bdl[d]	0.6	212	9,286	38,160	344,500
S105	La. Bajocian	Jura BL	Oosparite	25	ND	bdl[d]	1.5	47	1,448	1,713	391,200
S116	La. Bajocian	Jura BL	Oosparite	16	15	bdl[d]	1.4	72	1,067	1,709	408,800
S127	La. Bajocian	Jura BL	Oosparite	21	15	bdl[d]	1.3	34	1,242	1,518	405,700
S151	La. Bajocian	Jura BL	Oomicrite/sparite	92	324	bdl[d]	2.0	220	10,660	46,580	299,600
S153	La. Bajocian	Jura BL	Oomicrite/sparite	117	89	bdl[d]	1.0	266	4,465	14,060	373,400
S156	La. Bajocian	Jura BL	Oomicrite	480	381	5	4.2	247	2,977	9,812	390,700
La24BP3	Ea. Bajocian	Jura BL	Oomicrite	829	1,144	8	8.5	1,135	9,256	6,077	390,400
La24BP4	Ea. Bajocian	Jura BL	Oomicrite	606	690	7	5.5	1,149	7,007	12,050	387,000
Da4a	Ea. Bajocian	Burgundy	Biomicrite	145	105	bdl[d]	1.2	86	8,958	18,030	364,000
LU2	Ea. Bajocian	Burgundy	Biomicrite	344	240	5	2.7	268	8,135	9,602	382,600
LU1	Ea. Bajocian	Burgundy	Biomicrite	270	178	bdl[d]	bdl[d]	508	11,690	12,280	368,800
GUR	La. Bajocian	Jura NE	Oomicrite	43	ND	bdl[d]	ND	254	1,992	2,421	389,500
DOR	La. Oxfordian	Jura BL	Pelmicrite	207	ND	17	ND	6	413	748	386,600
Pi23	La. Oxfordian	Jura JU	Lagoonal micrite	40	38	bdl[d]	0.5	345	1,267	3,258	397,400
Pi17	La. Oxfordian	Jura JU	Lagoonal micrite	12	bdl[d]	bdl[d]	1.1	110	596	1,462	407,500

ND not determined

[a] *S* Schleifenberg, *La* Lausen, *Da* Davayé, *LU* Lucy-le-Bois, *GUR* Gurnigel, *DOR* Dornach, *Pi* Pichoux, see Fig. 2 for stratigraphical position of the samples

[b] *La* Late, *Ea* Early

[c] *BL* Canton Baselland, *NE* Canton Neuchâtel, *JU* Canton Jura

[d] *bdl* value below detection limit of 10 mg/kg for Zn_{ICP}, 5 mg/kg for Cd_{tot}, and 0.1 mg/kg for Cd_{ICP}

selected for further analysis, which also included the limestone bedrock samples from the soil profiles GUR and DOR. Geological properties and total contents of Zn, Fe, Si, S, Ca, and Cd (measured by XRF spectrometry) of these samples are listed in Table 1. Total Zn contents ranged from 12 to 829 mg/kg and in most cases were higher than acid-extractable Zn (Fig. 2; Table 1), in agreement with the "pseudo-total" character of acid-extractable Zn (see Sect. 2.2). Higher acid-extractable Zn content than total Zn content in some samples may be due to analytical error (possibly S32; 3 mg/kg difference) but more probably reflects the heterogeneity of the Zn distribution in the limestone (S151, La24). Limestone with total Zn contents above 200 mg/kg typically also contained at least 5 mg/kg of Cd [i.e., markedly higher than the 80-percentile level ($n = 37$) of 0.2 mg/kg Cd reported for limestone from Switzerland (Tuchschmid 1995)]. This qualitatively indicated a correlation between high Zn and Cd content.

3.2 Microscopic sedimentological description of selected limestone thin-sections

Among the limestone samples listed in Table 1, the samples S151, GUR and DOR were chosen for detailed

sedimentological description and microspectroscopic analyses. As inferred from microscopic observations, all three limestone samples were formed in an oolitic shoal environment. In relation to their lithofacies, the presence of echinoderms, brachiopods and bryozoans in various proportions suggests well-oxygenated water with normal salinity.

The S151 limestone from the Lausen–Schleifenberg section was defined as a partially recrystallised well-sorted oolitic grainstone, with concentric and radial-fibrous oolites ranging from 0.2 to 1.5 mm in diameter, most oolites being smaller than 0.5 mm (Fig. 3). Radial layers of oolites show partial micritisation. The oolites occur together with rare fragments of bivalve shells. The depositional setting is interpreted as a carbonate mid-ramp between the storm wave base and the fair-weather wave base. Important mechanical compaction seemed to have been hindered by rapid cementation, with granular cement partially dissolved and forming secondary porosity. Fractures, stylolithes, and structures of pressure-solution postdate cementation. Small partially oxidised grains of framboidal pyrite occur inside oolites, and especially at the rim and the contact between oolites. Ankerite crystals were observed in isolated micritic and marly matrix patches in concomitance with moderately rounded quartz and iron sulfide grains.

Fig. 3 Light microscope image of a thin-section from limestone S151 and corresponding μ-XRF maps for Zn, Fe and Ca. The mapped area is $3,000 \times 3,000 \; \mu m^2$ ($20 \times 20 \; \mu m^2$ resolution, 100 ms dwell time). The horizontally and vertically smeared-out signal around POI2 observed on the Zn distribution map is due to the intense Zn signal at this location, partially causing saturation of the detector
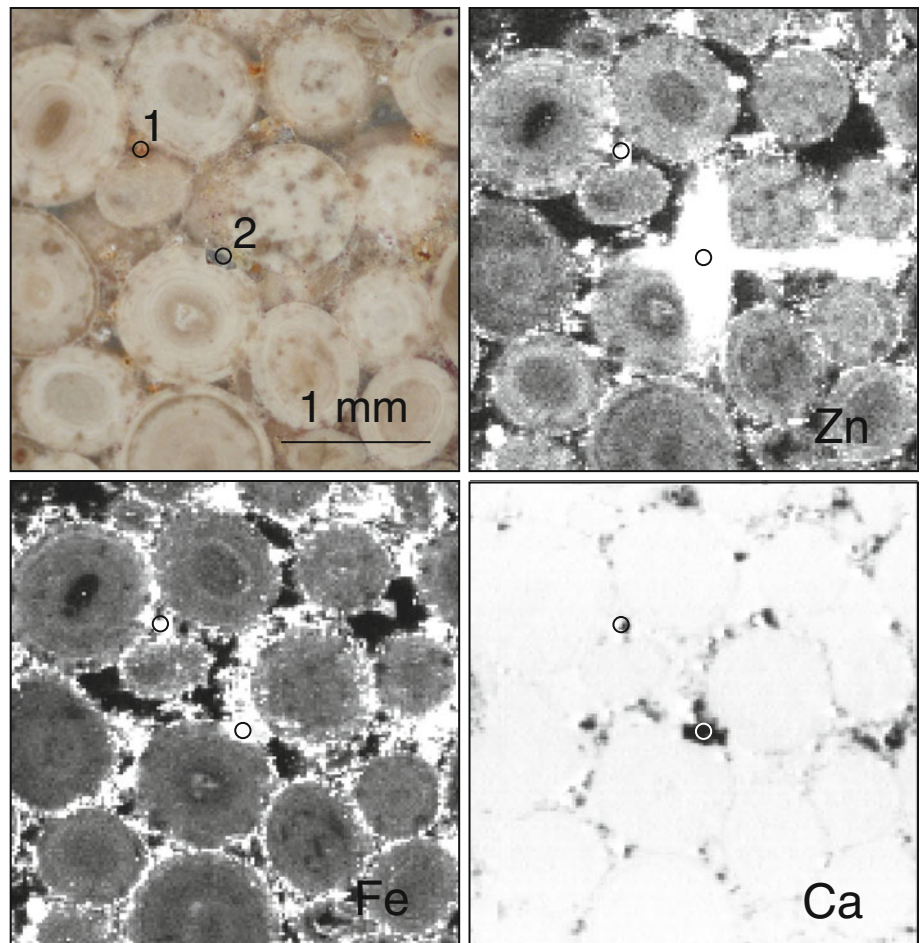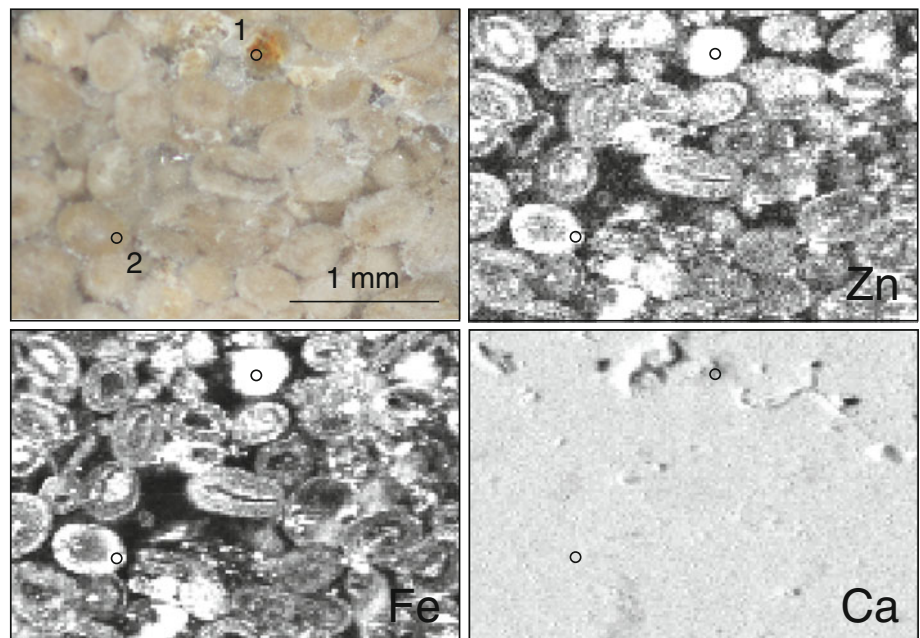
Fig. 4 Light microscope image of a thin-section from limestone GUR and corresponding μ-XRF maps for Zn, Fe and Ca. The mapped area is $3,000 \times 2,000 \; \mu m^2$ ($20 \times 20 \; \mu m^2$ resolution, 50 ms dwell time)

Concentric oolites and rare bioclasts classify the GUR limestone as oolitic grainstone (Fig. 4). The partially micritized oolites are well sorted and in part dissolved by a pressure-solution mechanism. Identified bioclasts are fragments of bivalves. The sediment was probably formed on the carbonate mid-ramp between the storm and

fair-weather wave bases. Interparticle pores are filled with granular cement. Diagenetic features are represented by stylolithes, pressure-solution and compaction structures, and partial recrystallisation. Partly altered iron sulfides occur in trace amounts both inside and around oolites as well as within stylolithes.

The well-sorted oolitic grainstone from DOR is slightly dolomitised and contains bioclasts (Fig. 5). The grains are mainly composed of micritized oolites as well as of concentric oolites and superficial oolites slightly smaller than 1 mm and partly dissolved. Gastropods and bivalve shells represent the main bioclasts. Reworked and broken oolites, bioturbation and abundant benthic fauna (bivalves, fragments of echinoderms) reflect sediment formation in a high-energy zone (oolite shoal, inner ramp environment) with important bacterial activity. Interparticle pores were filled with granular cement, with drusy cement completely transformed or dissolved during burial. During diagenesis the rock was partially recrystallized, the surface of oolites was corroded and partially dissolved, and small crystals of dolomite/ankerite were formed inside oolites. Other diagenetic features are fractures and structures of pressure-solution. Rarely, patches of Fe-(hydr)oxides can be observed in the rock.

3.3 Speciation of Zn in the limestone samples

The mineralogical speciation of Zn in the limestone samples listed in Table 1 was determined by bulk XANES spectroscopy at the Zn K-edge. In order to localize and better identify the different Zn-bearing phases, the distribution and speciation of Zn in thin-sections of the samples S151, GUR and DOR (Table 1) were analyzed using μ-XRF and μ-XANES spectroscopy.

3.3.1 Principal component analysis and target transform testing

The number of spectral components in the entire XANES data set (15 bulk and 5 μ-XANES spectra) was determined by PCA. The parameters of the first ten components obtained by PCA are given in Table 2. The empirical IND function reached a minimum with the first seven components, suggesting seven significant spectral components in the experimental spectra (Malinowski 1977). The first seven components described 98% of the total experimental variance.

Using the seven principal components from PCA and target transform testing (TT), potential reference spectra for LCF analysis were identified. The empirical SPOIL value (Malinowski 1978) and the NSSR of the respective target transforms (i.e., deviation between the experimental and the reconstructed spectra) were used to judge the suitability of the references. Results for selected reference spectra are provided in Table 3. Among all tested references, natural Zn-montmorillonite had the lowest SPOIL value whereas goethite with minor amounts of Zn substituting for Fe in the crystal lattice (Zn-goethite) was best reconstructed, as judged from its NSSR (Table 3; Fig. 6). Also sphalerite had a low NSSR and SPOIL value, whereas the SPOIL value of wurtzite (which contains Zn tetrahedrally coordinated to S as in sphalerite), was significantly higher. The similar local Zn coordination in sphalerite and wurtzite results in similar XANES spectra, which complicates distinction of these minerals in experimental Zn K-edge XANES spectra with several spectral contributions. Consequently, we only refer to ZnS in Table 4 reporting LCF results. The XANES spectra of sphalerite and wurtzite on the other hand largely differed from spectra of minerals such as Zn-goethite or Zn-calcite, in which Zn is octahedrally coordinated with O atoms (Fig. 6). Among the Zn-bearing carbonates in our database, hydrozincite and Zn-calcite had the lowest SPOIL and NSSR values. In contrast, the SPOIL value >6 of smithsonite indicated that this mineral was not relevant to the studied limestone samples. Zn-bearing Fe-(hydr)oxides, such as franklinite and Zn-ferrihydrite had a SPOIL value similar to that of Zn-goethite, but the high NSSR of their target transform suggested that these Zn phases were not dominant in the samples (Table 3; Fig. 6). Consequently, analysis of the experimental spectra by PCA and TT suggested that Zn phases forming under oxic (e.g., Zn-goethite) and reducing conditions (e.g., sphalerite) are relevant in the studied samples. This may indicate various changes in redox and pH conditions during rock formation and diagenesis.

3.3.2 Lausen–Schleifenberg

The distribution of Zn, Fe and Ca in a thin-section from the oolitic limestone S151 (Schleifenberg section, Early to Late Bajocian boundary) is shown in Fig. 3. Zn occurs concentrated in localized Zn-rich spots among the limestone cement and at the outermost rim of the oolites. The distribution of Zn was closely related to the distribution of Fe, but not to that of Ca. In localized Zn-rich spots next to oolites and in association with Fe, two different Zn phases were identified. At POI1, the respective XANES spectrum closely matched the spectrum of Zn-goethite (Fig. 6; Table 4). At POI2, an extremely high local Zn concentration resulted in an artificial horizontal and vertical "smearing out" of the Zn distribution pattern (Fig. 3) and severe distortion of the respective XANES spectrum by overabsorption (not shown). Nevertheless, the qualitative match of this spectrum to the spectrum of sphalerite suggested the presence of a massive ZnS grain at POI2. In line with the microspectroscopic results, the bulk spectrum of

Fig. 5 Light microscope image of a thin-section from limestone DOR and corresponding μ-XRF maps for Zn, Fe and Ca. The mapped area is $3{,}000 \times 2{,}000\ \mu m^2$ ($20 \times 20\ \mu m^2$ resolution, 10 ms dwell time)
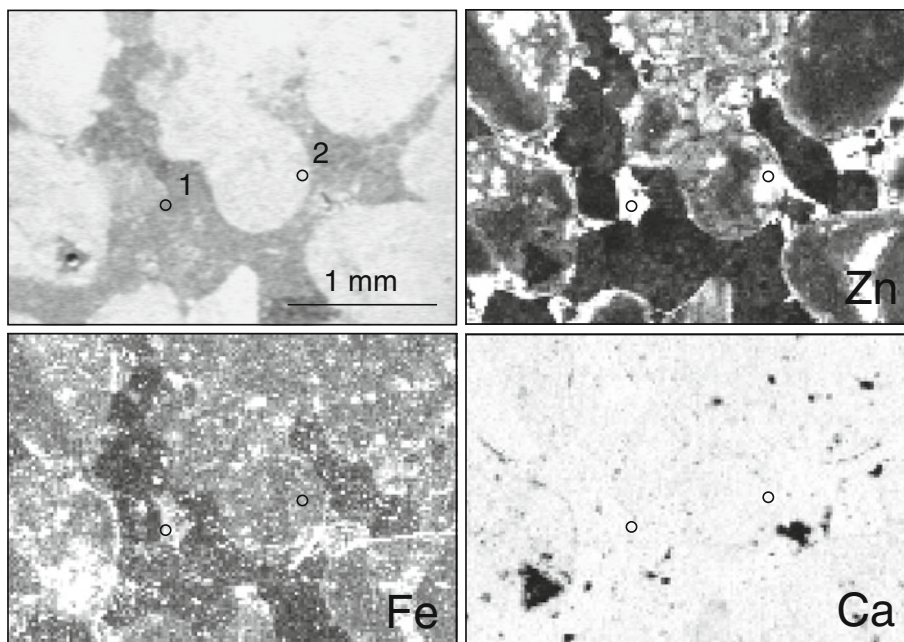

Table 2 Results from the principal component analysis of 20 bulk- and μ-XANES spectra collected on limestone powders and thin-sections

Component	Eigenvalue	Variance	Cum. var.[a]	IND[b]
1	136.1	0.876	0.876	0.00620
2	8.4	0.054	0.930	0.00358
3	4.4	0.028	0.959	0.00180
4	1.4	0.009	0.968	0.00157
5	1.0	0.006	0.974	0.00149
6	0.9	0.005	0.980	0.00135
7	0.6	0.003	0.984	0.00126
8	0.4	0.002	0.986	0.00132
9	0.3	0.002	0.988	0.00142
10	0.3	0.002	0.990	0.00154

[a] Cumulative variance

[b] Indicator function

sample S151 could be best reconstructed by sphalerite and Zn-goethite with a minor contribution from Zn-calcite (Fig. 6; Table 4). Earlier analysis of the same rock by bulk EXAFS spectroscopy gave similar results (Jacquat et al. 2009a).

The spectra of limestone S156 (Schleifenberg section, Early to Late Bajocian boundary) as well as La24BP3 and La24BP4 (Lausen section, Early to Late Bajocian boundary) resembled the spectrum of sample S151. Correspondingly, LCF analysis of these XANES spectra indicated sphalerite to be the major Zn phases together with a minor fraction of Zn-goethite. For sample La24BP3, addition of hemimorphite not only decreased the NSSR of the best LCF by more than 30%, but also visually improved

Table 3 Results from target transform testing of XANES reference spectra based on the seven principal components obtained by PCA (Table 2)

References	SPOIL[a]	NSSR (%)
nat. Zn-montmorillonite	1.2	0.02
Willemite	1.5	0.06
Zn-goethite	2.2	0.01
Franklinite	2.3	0.17
$Zn_{0.6}Mg_{0.4}$-kerolite	2.3	0.06
Sphalerite	2.4	0.02
$Zn_{0.34}Mg_{0.6}$-kerolite	2.7	0.08
Zn-ferrihydrite	2.9	0.12
$Zn_{0.8}Mg_{0.2}$-kerolite	3.0	0.07
Hydrozincite	3.0	0.03
Zn-calcite	3.1	0.03
Zn-hydroxide	3.4	0.04
Zn-kerolite	3.6	0.09
Wurtzite	3.9	0.05
$Zn_{0.06}Mg_{0.94}$-kerolite	3.9	0.10
Chalcophanite	3.9	0.13
Hemimorphite	4.6	0.15
syn. Zn-kaolinite	5.1	0.24
Gahnite	5.2	0.63
nat. Zn-kaolinite	5.4	0.18
Smithsonite	6.4	0.32
$ZnSO_4$	7.5	0.26
ZnO	7.6	0.40

Spectra are arranged by increasing SPOIL value. All listed references except $ZnSO_4$ and ZnO were included in the LCF analysis

[a] *SPOIL* 0–1.5 excellent; 1.5–3 good, 3–4.5 fair, 4.5–6 acceptable, >6 unacceptable reference (Malinowski 1978)

the reconstruction of the absorption edge. Euhedral crystals of hemimorphite ($Zn_4Si_2O_7(OH)_2 \cdot (H_2O)$) have previously been identified in limestone of the *garantiana* ammonite Zone (Late Bajocian) at the nearby location Orismühle close to Liestal (Offermann 1987).

The XANES spectra of the other Schleifenberg limestone samples located at the Early to Late Bajocian boundary (S153) or within the *niortense* (S127, S116, S105) and *parkinsoni* (S32) ammonite Zones of Late Bajocian were similar with a broad and pronounced edge shifted to higher energy compared to the sphalerite spectrum. In addition to Zn-goethite, the LCF of these spectra included minor fractions of Zn-calcite, sphalerite for sample S153, and hydrozincite for sample S105.

3.3.3 Vergisson–Davayé and Lucy-le-bois

LCF analysis of the XANES spectrum of a crinoid-rich limestone of the early Late Bajocian from the Davayé section (spectrum Da4a) indicated Zn-goethite to be the dominant Zn-phases (Table 4). The spectra of the limestone from Lucy-le-Bois (LU1 and LU2, Early Bajocian) resembled the Da4a spectrum. Consequently, mainly Zn-goethite and minor fractions of Zn-bearing carbonates (Zn-calcite, hydrozincite) were detected by LCF in these rocks (Table 4; Fig. 6).

3.3.4 Gurnigel

The light microscope image of a thin-section from the GUR oolitic limestone (Late Bajocian) and corresponding Zn, Fe, and Ca distribution maps are shown in Fig. 4. Similarly to the Schleifenberg limestone S151, the distribution of Zn resembled that of Fe. The μ-XANES spectra collected in the Zn–Fe rich matrix (GUR-1) as well as within an oolite rim (GUR-2) were best fitted with Zn-goethite. In the bulk spectrum, mainly Zn-goethite and a minor fraction of Zn-calcite were detected (Table 4; Fig. 6), in line with previous bulk EXAFS results on the same rock (Jacquat et al. 2009a).

3.3.5 Dornach

Distribution maps of Zn, Fe and Ca in a thin-section from the DOR oolitic limestone are shown in Fig. 5. The Zn distribution indicated localized Zn and Fe rich zones in the limestone cement and at the rim of the oolite. Similarly to the distribution of Zn in the limestone S151 and GUR, little or low concentrations of Zn were observed in the nucleus of the oolite. The μ-XANES spectra collected within the matrix (DOR-1) and the oolite rim (DOR-2) had a sharp edge followed by a smaller pronounced upward oscillation and were thus clearly different from the other collected

spectra. The spectra from the DOR oolitic limestone closely matched the Zn-calcite spectrum at both POIs (Table 4; Fig. 6), indicating that most Zn in this rock substituted for Ca in the crystal lattice of calcite. The bulk XANES spectrum of the sample DOR was contaminated by a signal from metallic Zn (not shown), but qualitatively confirmed that Zn-calcite was the major Zn phases in rock DOR. Similar results were obtained by bulk EXAFS spectroscopy (Jacquat et al. 2009a). The absence of sphalerite and Zn-goethite in sample DOR were in line with the very low contents of both Fe and S in this sample (Table 1).

3.3.6 Pichoux

The two spectra from the Pichoux section collected from oncoid-rich limestone of early Late Oxfordian age are clearly distinct, indicating a different local coordination of Zn in each rock. The spectrum Pi23 was best reconstructed with hydrozincite and minor contribution from Zn-calcite, whereas the spectrum Pi21 was best fitted by similar fractions of hydrozincite and Zn-calcite and a minor fraction of sphalerite (Table 4; Fig. 6).

4 Discussion

Measurements of the Zn content in limestone of Bajocian and Oxfordian age at different locations in the JMR and the Burgundy indicated that Zn is mostly associated with permeable carbonate levels and is inhomogeneously distributed both between as well as within the limestone beds. Numerous limestone layers had Zn concentrations above the 80-percentile level of 48 mg/kg reported for limestone from Switzerland (Tuchschmid 1995), with concentrations up to 3,576 mg/kg Zn, indicating anomalous elevated Zn concentration (Table 1 and Online Resource 1, Tables OR1–6). As identified by XANES spectroscopy, Bajocian limestone bore mainly sphalerite and/or Zn-substituted goethite and a minor fraction of Zn-carbonates, whereas Zn-bearing carbonates (Zn-calcite, hydrozincite) were accounting for most of the total Zn in the Oxfordian limestone. With respect to Bajocian limestone of the JMR, high Zn contents were reflected in a high fraction of sphalerite and low Zn contents in higher proportion of Zn-goethite, whereas Zn-goethite was the main Zn-bearing phase detected in Bajocian limestone from Burgundy independently of Zn content. In best LCF fits, sphalerite was always preferred over wurtzite (Table 4), but spectral interferences with minor fractions of wurtzite cannot be ruled out. Based on Zn-goethite and Zn-calcite fractions from LCF and total Zn, Ca and Fe contents of the selected limestone, the Zn contents in goethite and calcite were
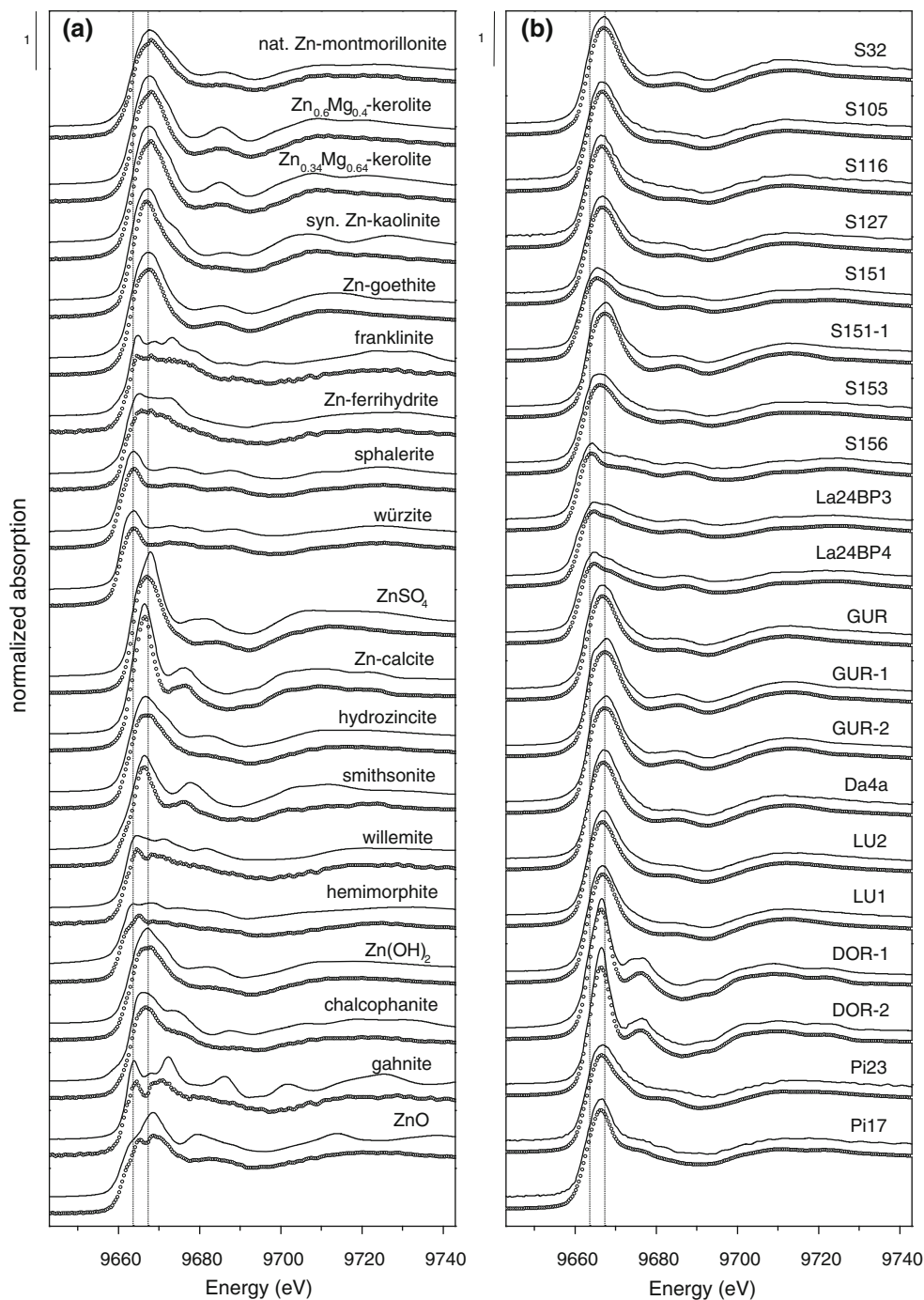
Fig. 6 a Zn K-edge XANES spectra of selected Zn reference compounds (*solid lines*) and respective target transforms (*dotted lines*, Table 3) calculated with the first 7 components from the principal component analysis of 20 rock XANES spectra (Table 2). **b** Bulk and μ-XANES spectra collected on selected limestone samples (*solid lines*) and corresponding LCF spectra (*dotted lines*). LCF results are provided in Table 4. *Vertical lines* at 9,663.6 and 9,667.3 eV mark the upper point of the ZnS and Zn-goethite *white lines*, respectively

estimated to range from 2,000 to 15,400 mg/kg and from 3 to 220 mg/kg, respectively.

There are at least four processes or combinations thereof which could explain the high Zn (and Cd) contents observed for the Jurassic limestone of the JMR and the

Burgundy: (1) continental fluvial inputs during sediment formation, (2) authigenic atmospheric fallouts from volcanic activities (Rambeau 2006), (3) inheritance of trace metals from nearby marly levels during diagenesis (Hofmann 1989; Hofmann and von Gehlen 1993),

Table 4 Best linear combination fit results for bulk and μ-XANES spectra of selected limestone samples

Spectrum	Zn-calcite (%)	Hydrozincite (%)	Zn-goethite (%)	Hemimorphite (%)	ZnS[a] (%)	Sum (%)	NSSR (‰)
S32	10	–	92	–	–	102	0.565
S105	16	42	39	–	–	97	0.170
S116	27	–	56	–	17	100	0.357
S127	15		66	–	16	98	0.295
S151	12	–	28	–	60	100	0.188
S151-1	–	–	101	–	–	101	0.460
S153	13	–	44	–	43	100	0.365
S156	–	–	13	–	86	99	0.334
La24BP3	–	–	22	21	58	101	0.412
La24BP4	–	–	29	–	72	101	0.127
Da4a	13	–	88	–	–	101	0.778
LU2	16	32	52	–	–	100	0.185
LU1	24	–	77	–	–	101	0.301
GUR	17	–	74	–	10	101	0.416
GUR-1	–	–	101	–	–	101	0.485
GUR-2	–	–	102	–	–	102	0.357
DOR-1	102	–	–	–	–	102	1.96
DOR-2	101	–	–	–	–	101	0.651
Pi17	39	42	–	–	17	98	0.328
Pi23	12	88	–	–	–	100	0.350

[a] Sphalerite was preferred over wurtzite in all best LCF

(4) hydrothermal input linked to tectonic activity (Efimenko et al. 2008).

The sporadicity and the presence of Zn peaks at similar age, e.g., at the boundary between the late Early Bajocian and early Late Bajocian, observed for the Lausen–Schleifenberg, Vergisson–Davayé and Lucy-le-Bois sections is in agreement with synsedimentary Zn inputs arising either from periodic continental pulses or from atmospheric fallouts. In that case, due to the high degree of water mixing in oolitic shoal environments, a homogeneous Zn distribution or at least the presence of Zn in all limestone components would be expected, with adsorption and incorporation of Zn into oolites. In sorption-dissolution experiments at room temperature, solid-state diffusion of adsorbed Zn and Fe into calcite particles have been reported to occur at rates of tens of angstroms to tens of nanometers per week (Mettler et al. 2009; Stipp et al. 1998). Assuming an average oolite radius of 0.8 mm for the investigated limestone, diffusion of Zn and Fe to the nucleus of pre-existing oolites may be expected within 1,500–15,000 years. The XRF maps collected in thin sections of the Schleifenberg and Gurnigel (Late Bajocian) and Dornach (Late Oxfordian) showed however that Zn (and Fe) is locally present in the limestone matrix and in some oolite rims. Little or no Zn had been detected in the nucleus of the oolites, with Zn having an irregular distribution rather than following the oolite lamination patterns. This distribution suggests that synsedimentary mechanisms involving Zn adsorption and diffusion were not major. Furthermore

and in discrepancy with a major process involving continental Zn input, no Zn-bearing clays were identified in the rocks. These observations suggest that the mechanism of Zn enrichment was rapid (less than a few ka) and not linked to oolite formation.

Inheritance of Zn principally from marly levels seems also unlikely since limestone layers with high Zn content showed little relation to the vicinity of marls (Fig. 2). Large variations in Zn content depending on sample position within a specific limestone layer (e.g., 24–3,580 mg/kg Zn within few centimeters depth for the La24 limestone bed) also preclude a major passive gradual enrichment pathway.

Concerning the fourth possibility—Zn enrichments due to hydrothermalism—it is worth noting that this interpretation is coherent with the stratigraphic sporadicity and microscale heterogeneity of the Zn distribution. In line with our Zn speciation results, several sphalerite mineralizations in permeable limestone levels of the Trias and Jurassic of the JMR have been previously reported (Hofmann 1989; Holenweg 1969). The sizes of sphalerite specimens (few millimeters to centimeters) described in these studies were however orders of magnitude larger than (sub-)micrometer-sized sphalerite grains observed here. From the analysis of facies changes and sediment thickness, episodic hydrothermal activity due to the reactivation of basement faults was postulated for the Bajocian/Bathonian and Oxfordian of the JMR (Allenbach 2001; Wetzel

et al. 2003). As fracture infills were not directly observed in the investigated limestone, the sphalerite micro-mineralizations may be related to a pervasive mechanism (or micro-scaled fluid paths) from nearby major faults (see Fig. 1 for fault and sample locations) and being constrained by the porosity and permeability of the rocks and the distance to the major faults. The cooling of the hydrothermal fluids that transport Zn either as Zn–Cl or Zn–H–S complexes was combined with a pH change towards more alkaline values due to interaction with the encasing carbonate rocks. Under the conditions experienced by the investigated limestone [maximal burial depth of 1,000 m and burial temperature of 70°C (Elie and Mazurek 2008; Mazurek et al. 2006; Timar-Geng et al. 2006)], these changes probably resulted in sphalerite precipitation (Daskalakis and Helz 1993; Tagirov et al. 2007). Recent direct Rb–Sr dating of sphalerite crystals from the Auenstein section (JMR, Late Bajocian/Early Bathonian) yielded an age of 162 ± 4 Ma, corresponding to Late Callovian/Early Oxfordian, which confirms that formation of sphalerite probably occurred after sediment deposition (Efimenko et al. 2009). In the nearby Black Forest and Vosges, hydrothermal ore deposits containing sphalerite were dated as Late Jurassic/Early Cretaceous but also to the Eocene/Oligocene formation of the Rheingraben structure (von Gehlen 1987). Detailed isotopic dating of sphalerite in the JMR would thus be needed to decipher the precise hydrothermalism chronology and evaluate links to the Black Forest and the Vosges.

The generally lower Zn content in limestone of Oxfordian age suggests less intense hydrothermal Zn input than for the underlying Bajocian strata, but the detection of sphalerite in the Pichoux section (Oxfordian) points to a similar enrichment mechanism. Following this interpretation, the presence of Zn-goethite could results from the oxidative transformation of framboidal pyrite (and/or siderite) and hydrothermal sphalerite in contact with meteoritic waters. Pyrite (as well as siderite) and sphalerite are particularly vulnerable to weathering under atmospheric conditions. In such conditions, the oxidation of the released Fe^{II} from pyrite will preferentially form goethite (Cornell and Schwertmann 1996). The higher redox potential in pores and oolite cortices than in the mineral matrix that supplies the Fe^{II} (Cornell and Schwertmann 1996) may have favoured the accumulation of Zn-goethite in voids and at the rim of oolites. The low burial temperature (max. 70°C) experienced by these Jurassic limestone (Elie and Mazurek 2008; Mazurek et al. 2006; Timar-Geng et al. 2006) would also preclude the formation of hematite from goethite. In support, evidence for secondary sulfide oxidation caused by the infiltration of oxygenated surface waters and post-dating Zn mineralizations in the Muschelkalk of the Black

forest has been inferred from sulfur isotope ratios (Hofmann and von Gehlen 1993). Furthermore, two major meteoric water inputs were linked to uplift events in Early Cretaceous (Barremian and Aptian/Albian, respectively) and the related exposures of the Burgundy platform (Brigaud et al. 2009). These palaeohydrological circulations brought a significant reduction of porosity (from 40 to 10%) through calcite cement precipitation (Brigaud et al. 2009). Linked with a minor pervasive hydrothermal input, these cementation processes may explain the heterogeneous distribution of Zn and the lack of a strong alteration of the rocks (buffering effect). In this context, grainstone with primary higher porosity than micritic limestone may favour sphalerite precipitation with subsequent oxidation to goethite, while formation of Zn-carbonates from Zn-rich hydrothermal fluids would be enhanced in limestone with low Fe and S content. This compares well with the total element content and Zn speciation results of the micritic limestone located in the inner ramp environment of the oolite shoal (e.g., Dornach Tables 1, 4; Fig. 6). Together with the spatial Zn heterogeneity, the difference in Zn speciation observed for Bajocian (mainly sphalerite and/or Zn-goethite) and Oxfordian (mainly Zn-carbonates) sections could thus arise from differences in rock permeability related to differences in rock facies (e.g., sparitic cement vs. micritic matrix in the oolitic limestone of Bajocian and Oxfordian age, respectively) or from the existence of several hydrothermal events showing variation in their age and composition. The possibility that some of the Zn contained in Zn-goethite and Zn-bearing carbonates has been already incorporated at the time of deposition cannot, however, be completely excluded.

Comparison between acid-extractable Zn and Cd contents of the selected limestone samples showed a strong correlation ($r = 0.97$, Online Resource 1, Fig. OR1, Table 1), pointing to a similar enrichment mechanism. This positive relationship between Cd and Zn contents in Jurassic limestone of the JMR and the Burgundy has previously been reported (Rambeau 2006). Sphalerite minerals from Jurassic limestone of the JMR have been shown to contain up to 18,000 mg/kg Cd (Efimenko et al. 2009). Similar to Zn, Cd could be hosted in calcite (Reeder 1996) and goethite (Huynh et al. 2003) and also otavite ($CdCO_3$) could form. More detailed mineralogical analyses of the respective limestone would be needed to determine the different Cd-bearing minerals and to relate Cd and Zn speciation.

The stratigraphically and spatially heterogeneous Zn distribution and the occurrence of sphalerite mineralizations indicates that hydrothermalism probably affected the JMR. In Bajocian limestone of the Burgundy, speciation results point to a similar enrichment mechanism as for the JMR. Detection of sphalerite mineralizations in the

Burgundy sequences are however called for to confirm that hydrothermalism was a main source of Zn (and Cd) in Jurassic limestone of the Burgundy.

5 Conclusions

Elevated Zn (and probably Cd) concentrations found in Bajocian and Oxfordian limestone of the JMR and in Bajocian carbonate sequences of the Burgundy were probably mainly caused by hydrothermal input. In this study, sphalerite and Zn-goethite (probably being a by-product of the oxidative dissolution of sphalerite and pyrite) in Bajocian limestone and Zn-calcite and hydrozincite in Oxfordian limestone were the main Zn phases identified. Difference in speciation between oolitic sparitic limestone of Bajocian age and bioclastic micritic limestone of Oxfordian age may be related to differences in rock permeability, i.e., rock facies, and/or to various hydrothermal events. Isotopic dating of the different mineralizations will be needed to decipher differences in Bajocian and Oxfordian Zn speciation and to precise the hydrothermalism chronology. The results of this study may also help to specifically map potential soils having geogenically elevated Zn and Cd contents.

References

Allenbach, R. P. (2001). Synsedimentary tectonics in an epicontinental sea: A new interpretation of the Oxfordian basins of northern Switzerland. *Eclogae Geologica Helvetica, 94*, 265–287.

Alloway, B. J. (1995). *Heavy metals in soils*. London: Chapman & Hall.

Baize, D., & Sterckeman, T. (2001). Of the necessity of knowledge of the natural pedo-geochemical background content in the evaluation of the contamination of soils by trace elements. *The Science of the Total Environment, 264*, 127–139.

Beauchemin, S., Hesterberg, D., Nadeau, J., & McGeer, J. C. (2004). Speciation of hepatic Zn in trout exposed to elevated waterborne Zn using X-ray absorption spectroscopy. *Environmental Science and Technology, 38*, 1288–1295.

Brigaud, B., Durlet, C., Deconinck, J.-F., Vincent, B., Thierry, J., & Trouiller, A. (2009). The origin and timing of multiphase cementation in carbonates: Impact of regional scale geodynamic events on the Middle Jurassic Limestones diagenesis (Paris Basin, France). *Sedimentary Geology, 222*, 161–180.

Chevalier, G., Diamond, L., & Leu, W. (2010). Potential for deep geological sequestration of CO_2 in Switzerland: A first appraisal. *Swiss Journal of Geosciences, 103*, 427–455.

Cornell, R. M., & Schwertmann, U. (1996). *The iron oxides*. New York: Wiley VCH.

Daskalakis, K. D., & Helz, G. R. (1993). The solubility of sphalerite (ZnS) in sulfidic solutions at 25°C and 1 atm pressure. *Geochimica et Cosmochimica Acta, 57*, 4923–4931.

Dubois, J.-P., Benitez, N., Liebig, T., Baudraz, M., & Okopnik, F. (2002). Le cadmium dans les sols du Haut Jura Suisse. In D. Baize & M. Tercé (Eds.), *Les Eléments Traces Métalliques dans les Sols: Approches Fonctionnelles et Spatiales*. Orléans: INRA.

Efimenko, N., Matera, V., Adatte, T., & Föllmi, K. (2008). Cadmium anomalies in Jurassic carbonates in western and southern Europe: Towards the causes and mechanisms. *Geophysical Research Abstracts, 10*, A-09829.

Efimenko, N., Spangenberg, J., Schneider, J., Adatte, T., Matera, V., & Föllmi, K. (2009). Sphalerite mineralisation in Bajocian shallow-water carbonates in the Swiss Jura Mountains related to extensional synsedimentary tectonics during the Middle-Late Jurassic. In 7th Swiss geoscience meeting, Neuchâtel, Switzerland. http://geoscience-meeting.scnatweb.ch/sgm2009/SGM09_Abstracts/PDF/SGM_n2009_Symposium3.pdf.

Elie, M., & Mazurek, M. (2008). Biomarker transformations as constraints for the depositional environment and for maximum temperatures during burial of Opalinus Clay and Posidonia Shale in northern Switzerland. *Applied Geochemistry, 23*, 3337–3354.

Gleyzes, C., Tellier, S., & Astruc, M. (2002). Fractionation studies of trace elements in contaminated soils and sediments: A review of sequential extraction procedures. *TrAC-Trends in Analytical Chemistry, 21*, 451–467.

Gonzalez, R., & Wetzel, A. (1996). Stratigraphy and paleogeography of the Hauptrogenstein and Klingnau Formations (middle Bajocian to late Bathonian), northern Switzerland. *Eclogae geologica Helvetica, 89*, 695–720.

Hofmann, B. (1989). Erzmineralien in paläozoischen, mesozoischen und tertiären Sedimenten der Nordwestschweiz und Südwestdeutschland. *Schweizerische Mineralogische Petrographische Mitteilungen, 69*, 345–357.

Hofmann, B., & von Gehlen, K. (1993). Formation of stratiform sulfide mineralizations in the Lower Muschelkalk (Middle Triassic) of Southwestern Germany and Northern Switzerland: Constraints from sulfur isotope data. *Schweizerische Mineralogische Petrographische Mitteilungen, 73*, 365–374.

Holenweg, H. (1969). Mineralparagenesen im Schweizer Jura. *Schweizer Strahler, 4*, 303–308.

Hug, W. A. (2003). Sequenzielle Faziesentwicklung der Karbonatplattform des Schweizer Jura im späten Oxford und frühesten Kimmeridge. *Ph.D. thesis*, University of Fribourg, Switzerland.

Huynh, T., Tong, A. R., Singh, B., & Kennedy, B. J. (2003). Cd-substituted goethites—a structural investigation by synchrotron X-ray diffraction. *Clays and Clay Minerals, 51*, 397–402.

Isaure, M.-P., Laboudigue, A., Manceau, A., Sarret, G., Tiffrau, C., Trocellier, P., et al. (2002). Quantitative Zn speciation in a contaminated dredged sediment by μ-PIXE, μ-SXRF, EXAFS spectroscopy and principal component analysis. *Geochimica et Cosmochimica Acta, 66*, 1549–1567.

Jacquat, O., Voegelin, A., Juillot, F., & Kretzschmar, R. (2009a). Changes in Zn speciation during soil formation from Zn-rich limestones. *Geochimica et Cosmochimica Acta, 73*, 5554–5571.

Jacquat, O., Voegelin, A., & Kretzschmar, R. (2009b). Local coordination of Zn in hydroxy-interlayered minerals and implications for Zn retention in soils. *Geochimica et Cosmochimica Acta, 73*, 348–363.

Jacquat, O., Voegelin, A., & Kretzschmar, R. (2009c). Soil properties controlling Zn speciation and fractionation in contaminated soils. *Geochimica et Cosmochimica Acta, 73*, 5256–5272.

Jacquat, O., Voegelin, A., Villard, A., Marcus, M. A., & Kretzschmar, R. (2008). Formation of Zn-rich phyllosilicates, Zn-layered double hydroxide and hydrozincite in contaminated calcareous soils. *Geochimica et Cosmochimica Acta, 72*, 5034–5057.

Kelly, S. D., Hesterberg, D., & Ravel, B. (2008). Analysis of soils and minerals using X-ray absorption spectroscopy. In A. L. Ulery, & R. Drees (Eds.), *Methods of Soil Analysis. Part 5—Mineralogical Methods*. Madison: Soil Science Society of America.

Kirpichtchikova, T. A., Manceau, A., Spadini, L., Panfili, F., Marcus, M. A., & Jacquet, T. (2006). Speciation and solubility of heavy metals in contaminated soil using X-ray microfluorescence, EXAFS spectroscopy, chemical extraction, and thermodynamic modeling. *Geochimica et Cosmochimica Acta, 70*, 2163–2190.

Koningsberger, D. C., & Prins, R. (1988). *X-ray absorption: Principles, applications, techniques of EXAFS, SEXAFS, XANES*. New York: Wiley.

Laveuf, C., Cornu, S., Baize, D., Hardy, M., Josiere, O., Drouin, S., et al. (2009). Zinc redistribution in a soil developed from limestone during pedogenesis. *Pedosphere, 19*, 292–304.

Malinowski, E. R. (1977). Determination of the number of factors and the experimental error in a data matrix. *Analytical Chemistry, 49*, 612–617.

Malinowski, E. R. (1978). Theory of error for target factor analysis with applications to mass spectrometry and nuclear magnetic resonance spectrometry. *Analytica Chimica Acta, 103*, 339–354.

Manceau, A., Marcus, M. A., & Tamura, N. (2002). Quantitative speciation of heavy metals in soils and sediments by synchrotron X-ray techniques. In P. A. Fenter, M. L. Rivers, N. C. Sturchio, & S. R. Sutton (Eds.), *Application of synchrotron radiation in low-temperature geochemistry and environmental science*. Washington, DC: Mineralogical Society of America.

Manceau, A., Tamura, N., Celestre, R. S., MacDowell, A. A., Geoffroy, N., Sposito, G., et al. (2003). Molecular-scale speciation of Zn and Ni in soil ferromanganese nodules from loess soils of the Mississippi Basin. *Environmental Science and Technology, 37*, 75–80.

Marcus, M. A., MacDowell, A. A., Celestre, R. S., Manceau, A., Miler, T., Padmore, H. A., et al. (2004). Beamline 10.3.2 at ALS: A hard X-ray microprobe for environmental and materials science. *Journal of Synchrotron Radiation, 11*, 239–247.

Mazurek, M., Hurford, A. J., & Leu, W. (2006). Unravelling the multi-stage burial history of the Swiss Molasse Basin: Integration of apatite fission track, vitrinite reflectance and biomarker isomerisation analysis. *Basin Research, 18*, 27–50.

Mégnien, C., Mégnien, F., Turland, M., & Villalard, P. (1971). Carte géologique de la France au 1:50'000, feuille Vermenton. *Bull. BRGM, XXVII*(21).

Mettler, S., Wolthers, M., Charlet, L., & von Gunten, U. (2009). Sorption and catalytic oxidation of Fe(II) at the surface of calcite. *Geochimica et Cosmochimica Acta, 73*, 1826–1840.

Offermann, E. (1987). Hemimorphit…erstmals aus dem Schweizer Jura! *Schweizer Strahler, 7*, 418.

Panfili, F. R., Manceau, A., Sarret, G., Spadini, L., Kirpichtchikova, T., Bert, V., et al. (2005). The effect of phytostabilization on Zn speciation in a dredged contaminated sediment using scanning electron microscopy, X-ray fluorescence, EXAFS spectroscopy, and principal components analysis. *Geochimica et Cosmochimica Acta, 69*, 2265–2284.

Quezada-Hinojosa, R. P., Matera, V., Adatte, T., Rambeau, C., & Föllmi, K. B. (2009). Cadmium distribution in soils covering Jurassic oolitic limestone with high Cd contents in the Swiss Jura. *Geoderma, 150*, 287–301.

Rambeau, C. (2006). Cadmium anomalies in Jurassic carbonates (Bajocian, Oxfordian) in western and southern Europe. *Ph.D. thesis*, University of Neuchâtel, Switzerland.

Rambeau, C., Baize, D., Saby, N., Matera, V., Adatte, T., & Föllmi, K. B. (2010). High cadmium concentrations in Jurassic limestone as the cause for elevated cadmium levels in deriving soils: A case study in Lower Burgundy, France. *Environmental Earth Sciences, 61*, 1575–1585.

Ravel, B., & Newville, M. (2005). Athena, Artemis, Hephaestus: Data analysis for X-ray absorption spectroscopy using IFEFFIT. *Journal of Synchrotron Radiation, 12*, 537–541.

Reeder, R. J. (1996). Interaction of divalent cobalt, zinc, cadmium, and barium with the calcite surface during layer growth. *Geochimica et Cosmochimica Acta, 60*, 1543–1552.

Sarret, G., Balesdent, J., Bouziri, L., Garnier, J. M., Marcus, M. A., Geoffroy, N., et al. (2004). Zn speciation in the organic horizon of a contaminated soil by micro-X-ray fluorescence, micro- and powder-EXAFS spectroscopy, and isotopic dilution. *Environmental Science and Technology, 38*, 2792–2801.

Spicher, A. (2005). Geologische Karte der Schweiz, 1:500 000. Bern: Bundesamt für Landestopographie (swisstopo).

Stipp, S. L. S., Konnerup-Madsen, J., Franzreb, K., Kulik, A., & Mathieu, H. J. (1998). Spontaneous movement of ions through calcite at standard temperature and pressure. *Nature, 396*, 356–359.

Tagirov, B. R., Suleimenov, O. M., & Seward, T. M. (2007). Zinc complexation in aqueous sulfide solutions: Determination of the stoichiometry and stability of complexes via ZnS(cr) solubility measurements at 100°C and 150 bars. *Geochimica et Cosmochimica Acta, 71*, 4942–4953.

Thierry, J., & Barrier, E. (2000). Middle Callovian. In J. Dercourt, M. Gaetani, B. Vrielvynck, E. Barrier, B. Biju-Duval, M. F. Brunet, J. P. Cadet, S. Crasquin, & M. Sandulescu (Eds.), *Atlas Peri-Tethys*, Paris.

Thiry-Bastien, P. (2002). Stratigraphie séquentielle des calcaires bajociens de l'Est de la France (Jura—Bassin de Paris). *Ph.D. thesis*, University Claude Bernard Lyon, France.

Timar-Geng, Z., Fügenschuh, B., Wetzel, A., & Dresmann, H. (2006). The low-temperature thermal history of northern Switzerland as revealed by fission track analysis and inverse thermal modelling. *Eclogae Geologica Helvetica, 99*, 255–270.

Tuchschmid, M. P. (1995). Quantifizierung und Regionalisierung von Schwermetall- und Fluorgehalten bodenbildender Gesteine der Schweiz. Umwelt Materialen 32, Bundesamt für Umwelt, Wald und Lanschaft, Bern, Switzerland.

Voegelin, A., Tokpa, G., Jacquat, O., Barmettler, K., & Kretzschmar, R. (2008). Zinc fractionation in contaminated soils by sequential and single extractions: Influence of soil properties and zinc content. *Journal of Environmental Quality, 37*, 1190–1200.

von Gehlen, K. (1987). Formation of Pb-Zn-F-Ba mineralizations in SW Germany: A status report. *Fortschritte der Mineralogie, 65*, 87–113.

Webb, S. M. (2005). SIXPack: A graphical user interface for XAS analysis using IFEFFIT. *Physica Scripta, T115*, 1011–1014.

Wetzel, A., Allenbach, R., & Allia, V. (2003). Reactivated basement structures affecting the sedimentary facies in a tectonically "quiescent" epicontinental basin: An example from NW Switzerland. *Sedimentary Geology, 157*, 153–172.